

# Microstructural and electrical characterizations of tungsten-doped $\text{La}_2\text{Mo}_2\text{O}_9$ prepared by spray pyrolysis

Laura Baqué · Jesús Vega-Castillo · Samuel Georges · Alberto Caneiro · Elisabeth Djurado

Received: 4 February 2013 / Revised: 10 April 2013 / Accepted: 5 May 2013 / Published online: 4 June 2013  
© Springer-Verlag Berlin Heidelberg 2013

**Abstract**  $\text{La}_2\text{Mo}_{2-x}\text{W}_x\text{O}_9$  ( $x=0, 0.5, 1.0,$  and  $1.3$ ) nanocrystalline powders were synthesized by spray pyrolysis (SP) assisted by an ultrasonic atomizer. Microstructure, sinterability and thermal stability of the prepared powders were investigated. Spherical particles of 430 to 530 nm in diameter and crystallite sizes in the 30–44 nm range were obtained. Additionally, the fine microstructure has allowed the reduction of sintering temperatures with respect to that usually reported for a solid-state reaction (SSR) method. Pellets with a variety of average grain sizes and morphologies were obtained by applying different sintering programs starting from  $\text{La}_2\text{Mo}_{2-x}\text{W}_x\text{O}_9$  powders ( $x=0$  and  $1.3$ ) obtained by SP and SSR processes. The electrical properties of these ionic conductors were analyzed by Electrochemical Impedance Spectroscopy (EIS) and correlated with microstructural observations. No significant variation of the electrical properties of these ionic conductors was

found as compared to conventional ceramics with remarkable microstructural differences.

**Keywords** SOFC · LAMOX · Spray pyrolysis · Spark plasma sintering

## Introduction

Solid oxide fuel cells (SOFCs) can convert chemical energy from hydrogen and oxygen into electrical energy in an environment-friendly manner for a wide power range. Nevertheless, the practical application of these devices is hindered by the high operation temperature (up to 800 °C) required to allow the conduction of oxygen ions through conventional electrolytes (i.e., yttria-stabilized zirconia (YSZ)) [1].

The use of new electrolyte materials with high ionic conductivity would reduce the cell operation temperature [1, 2].  $\text{La}_2\text{Mo}_2\text{O}_9$  undergoes a reversible transition from monoclinic  $\alpha$  to cubic  $\beta$  structure at  $\sim 580$  °C, leading to an increase of the ionic conductivity up to two orders of magnitude and reaching values higher than those corresponding to YSZ [3]. However, a limitation for considering  $\text{La}_2\text{Mo}_2\text{O}_9$  as an electrolyte material for SOFCs is its stability in reducing atmospheres [4]. In this respect, the substitution of Mo by W (i.e.,  $\text{La}_2\text{Mo}_{2-x}\text{W}_x\text{O}_9$ ) has been reported to improve the stability against reduction of this kind of materials with a slight decrease of ionic conductivity [5]. Another effect of W doping is the suppression of the  $\alpha \leftrightarrow \beta$  transition, retaining the high temperature  $\beta$ -cubic phase [3, 6].

On the other hand, several authors reported an ionic conductivity enhancement when decreasing crystallite size to the nano- or sub-micrometer range [7–10]. In particular, it is very difficult to prepare nanostructured materials in a dense form as it is required by SOFC electrolytes. Accordingly, most of the studies reported in the literature regarding  $\text{La}_2\text{Mo}_{2-x}\text{W}_x\text{O}_9$

L. Baqué · J. Vega-Castillo · A. Caneiro  
Centro Atómico Bariloche, Instituto Balseiro, Av. Bustillo 9500,  
8400, San Carlos de Bariloche, RN, Argentina

L. Baqué · J. Vega-Castillo · A. Caneiro  
Consejo Nacional de Investigaciones Científicas y Técnicas  
(CONICET), Buenos Aires, Argentina

S. Georges · E. Djurado  
LEPMI, UMR 5279, CNRS, Grenoble INP, Université de Savoie–  
Université Joseph Fourier, BP75,  
38402 Saint Martin d'Hères, France

A. Caneiro (✉)  
Comisión Nacional de Energía Atómica CNEA, Buenos Aires,  
Argentina  
e-mail: caneiro@cab.cnea.gov.ar

L. Baqué  
DTU Energy Conversion, Risoe Campus, Frederiksborgvej 399,  
4000 Roskilde, Denmark

focus on crystal structure, thermal stability, and electrical properties of dense ceramics with micrometer-sized grains [5, 6, 11–13]. Nevertheless, some authors have demonstrated that some sintering methods such as fast firing (i.e., thermal treatment at high temperature for a short period of time) [14], spark plasma sintering (SPS) [15], or Chen-type sintering [8] are adequate to obtain dense nanostructured materials. For that reason, the comprehensive microstructure, thermal stability, and sinterability characterization of starting powders are important in order to select the optimal synthesis and sintering parameters for the elaboration of dense nanostructured ceramics.

The routes reported in the literature to obtain nanocrystalline  $\text{La}_2\text{Mo}_2\text{O}_9$ -based oxide powders include the citrate method [15], freeze-drying method [16], and Pechini-derived methods [8, 17]. These procedures usually involve several steps which take several hours or even days to achieve the complete phase formation. In contrast, spray pyrolysis (SP) technique is low-cost and suitable for obtaining homogeneous spherical nanoscaled particles with good purity within short reaction times of pyrolysis, typically less than 10 s and with a precise reproducibility. For instance, Georges et al. have reported the synthesis and characterization of nanocrystalline pure  $\text{La}_2\text{Mo}_2\text{O}_9$  powders by SP [14].

In this process, the dissolved precursor salts were ultrasonically aerosolized, and then, as evaporation of water solvent proceeded, solute precipitation occurred within droplets when the critical supersaturation solute concentration was achieved. This was followed by drying, thermolysis of the precipitates, and eventually sintering at high temperatures to form amorphous or polycrystalline spherical ultrafine alumina particles.

The present work deals with the synthesis of  $\text{La}_2\text{Mo}_2 - x\text{W}_x\text{O}_9$  ( $x=0, 0.5, 1.0, \text{ and } 1.3$ ) powders with controlled microstructure by SP. Nano/microstructure, sinterability, and thermal stability of the obtained powders are investigated and compared with those data from the literature.

The electrical properties of  $\text{La}_2\text{Mo}_2\text{O}_9$  and  $\text{La}_2\text{Mo}_{0.7}\text{W}_{1.3}\text{O}_9$  electrolytes sintered by SPS and conventional sintering for different periods and temperatures starting from SP and solid-state reaction (SSR) powders have been studied by electrochemical impedance spectroscopy (EIS) and compared. Structural and morphological properties of the pellets were analyzed.

## Experimental part

Stoichiometric amounts of  $\text{La}(\text{NO}_3)_3 \cdot 6 \text{H}_2\text{O}$  (99.9 %, Alfa Aesar),  $(\text{NH}_4)_6\text{Mo}_7\text{O}_{24} \cdot 4 \text{H}_2\text{O}$  (>99 %, Sigma-Aldrich), and  $(\text{NH}_4)_6\text{W}_{12}\text{O}_{39} \cdot y \text{H}_2\text{O}$  (Sigma-Aldrich) were separately dissolved in distilled water. Cation concentrations were fixed to  $[\text{La}^{3+}] = [\text{Mo}^{6+}] + [\text{W}^{6+}] = 0.025 \text{ M}$ . Some droplets

of  $\text{HNO}_3$  were added to  $(\text{NH}_4)_6\text{Mo}_7\text{O}_{24}$  and  $(\text{NH}_4)_6\text{W}_{12}\text{O}_{39}$  solutions in order to set the pH to that of the  $\text{La}(\text{NO}_3)_3$  solution. Afterwards, these three solutions were mixed, and an appropriated amount of hydrogen peroxide was added to stabilize the final solution.

The obtained  $\text{La}_2\text{Mo}_2 - x\text{W}_x\text{O}_9$  ( $x=0, 0.5, 1.0, \text{ and } 1.3$ ) solutions were atomized separately at 1.7 MHz using a high-frequency ultrasonic generator with three ceramic transducers. The produced aerosol was carried using an 80 %  $\text{N}_2$  and 20 %  $\text{O}_2$  gas mixture with a flow rate of  $6 \text{ L min}^{-1}$  through a three-zone tubular furnace (Carbolite TZF, 60 mm in diameter and 1,090 mm in heated length) heated at  $600 \text{ }^\circ\text{C}$ . Then, the powders were collected in an electrostatic receptor at 10 kV located at the furnace exit. Spray pyrolysis experimental setup was detailed elsewhere [14].

A second batch of  $\text{La}_2\text{Mo}_2 - x\text{W}_x\text{O}_9$  powders was prepared by conventional SSR using stoichiometric amounts of decarbonated  $\text{La}_2\text{O}_3$  (>99.5 %, Merck),  $\text{MoO}_3$ , and  $\text{WO}_3$  (99.8 %, Alfa Aesar) ground in ethanol. After evaporation, the mixture was annealed once at  $500 \text{ }^\circ\text{C}$  and twice at  $1,000 \text{ }^\circ\text{C}$  for 24 h each, with heating and cooling rates of  $5 \text{ }^\circ\text{C min}^{-1}$  in air. Intermediate grindings were performed in order to reach a full solid-state reaction.

The morphology of  $\text{La}_2\text{Mo}_2 - x\text{W}_x\text{O}_9$  powders and dense ceramics was observed by high-resolution scanning electron microscopy (SEM, ZEISS Ultra 55). Statistical analysis was made measuring individual particle diameter from SEM images with an uncertainty of  $\pm 40 \text{ nm}$ .

X-ray diffraction data were collected at room temperature using the PANalytical Bragg–Brentano X'Pert PRO MPD diffractometer equipped with the X'Celerator detector, using  $\text{Cu K}\alpha$  radiation in the  $10^\circ \leq 2\theta \leq 90^\circ$  range with a two-theta step of  $0.017^\circ$  and 150 s counting time. The analysis of X-ray diffraction (XRD) patterns was performed using the Le Bail (or whole-pattern decomposition) refinement [18] with constant scale factors as implemented in the FullProf package [19, 20].  $\text{La}_2\text{Mo}_2 - x\text{W}_x\text{O}_9$  patterns were indexed in  $\text{P2}_1$  space group for  $x=0$  and  $\text{P2}_13$  for  $x=0.5, 1, \text{ and } 1.3$ . The initial cell parameters were taken from Goutenoire et al. [21] (for  $x=0$ ) and Corbel et al. [11] (for  $x=0.5, 1, \text{ and } 1.3$ ). Microstructural effects (average crystallite size and strain) were analyzed using an isotropic size and strain broadening model as implemented in the FullProf package [20]. More details regarding the procedure and algorithms used for this analysis were reported elsewhere [14].

Thermal stability and decomposition of  $\text{La}_2\text{Mo}_2 - x\text{W}_x\text{O}_9$  powders were studied in air by differential thermal analysis (DTA) and thermogravimetric analysis (TGA) using the Netzsch STA 409 PC/PG thermobalance, with heating and cooling rates of  $10 \text{ K min}^{-1}$  in the  $20\text{--}1,000 \text{ }^\circ\text{C}$  temperature range, with  $\text{Al}_2\text{O}_3$  as thermal reference.

Thermal shrinkage of  $\text{La}_2\text{Mo}_2 - x\text{W}_x\text{O}_9$  pellets was monitored by dilatometric analysis using the Netzsch 402-C

dilatometer in air with heating and cooling rates of  $5 \text{ K min}^{-1}$ . In order to perform this experiment, the as-prepared powders were uniaxially pressed to form cylindrical pellets, and afterward, a pressure of 2,500 bar was isostatically applied to relax residual tensions.

Dense ceramic samples were prepared starting from both SP and SSR  $\text{La}_2\text{Mo}_2 - x\text{W}_x\text{O}_9$  powders with  $x=0$  and 1.3. A decrease of particles sizes was achieved by ball milling for four periods of 15 min with intervals of 15 min for cooling. Cylindrical green pellets were shaped by pressing  $\text{La}_2\text{Mo}_2 - x\text{W}_x\text{O}_9$  powders first uniaxially under 100 MPa and then isostatically under 250 MPa. Different sintering techniques were applied onto five prepared pellets as in conditions previously determined by dilatometry. Solid-state reaction pellets with  $x=0$  and 1.3 (labeled SSR00 and SSR13, respectively) were sintered at high temperatures (1,070 and 1,300 °C, respectively) for 2 h. SP ceramics (SP00 and SP13) were sintered for shorter times (10 and 1 min, respectively) at 970 and 1,090 °C, respectively. A second SP pellet with  $x=0$  (SPS00) was pre-annealed at 700 °C for 2 h in air and then sintered by SPS in the SPS apparatus type HP D 25/1 (FCT GmbH, Germany). The SP  $\text{La}_2\text{Mo}_2\text{O}_9$  powder was placed in a graphite die ( $\varnothing 20 \text{ mm}$ ), and the electric current of  $\sim 1,000 \text{ A}$  was applied through the graphite die. The applied pressure was 75 MPa. The heating rate was set to  $100 \text{ K min}^{-1}$  up to 700 °C for a dwelling time of 2 min, in order to avoid any decomposition of the pellet. Then, the cooling rate was set to  $100 \text{ K min}^{-1}$  down to 600 °C and then naturally cooled down to room temperature. An attempt of SPS sintering was also made on the SP  $\text{La}_2\text{Mo}_{0.7}\text{W}_{1.3}\text{O}_9$  pellet (SPS13); unfortunately, the sintered pellet was broken after the process and could not be characterized. In order to characterize the microstructure of sintered SSR00, SP00, SPS00, SSR13, and SP13 ceramics by SEM, the pellets were fractured, polished, and thermally etched at 50 °C below their respective sintering temperature for 30 min.

$\text{La}_2\text{Mo}_2 - x\text{W}_x\text{O}_9$  ceramics, with different microstructures, were analyzed by EIS using the Hewlett-Packard 4192A LF frequency response analyzer. Platinum electrodes were deposited by sputtering onto both flat faces of SP00, SP13, SSR00, and SSR13 pellets. EIS spectra were collected in air between 295 and 700 °C within a frequency range from 13 MHz to 5 Hz and voltage amplitude of 50 mV. A thermal stabilization time of at least 30 min was applied between each measurement.

The spectra were fitted using resistance in parallel with a constant phase element ( $R||\text{CPE}$ ) circuits for modeling of high- and intermediate-frequency semicircles assigned to the electrolyte responses (bulk and grain boundary contributions of the electrolyte response). The low-frequency

range of the spectra, due to the Pt electrodes reaction, was modeled arbitrarily with the Warburg element, in order to account for the whole electrochemical cell and to avoid errors due to partial convolution of electrical and electrochemical domains of the spectra.

## Results

### Morphology of SP $\text{La}_2\text{Mo}_2 - x\text{W}_x\text{O}_9$ powders

SEM micrographs of the SP powders with different tungsten contents are presented on the left part of Fig. 1. Statistical analysis of particle size made on these micrographs is shown in the graphs on the right-hand side of Fig. 1. In addition, volumetric distribution (presented in the graph inset) was calculated, assuming perfect and dense spheres. The number of measured particles, arithmetic average, standard deviation, and mode resulting from this analysis are summarized in Table 1.

As observed on the SEM micrographs (Fig. 1), the four as-prepared powders present spherical solid particles as observed usually for SP [14, 22]. Indeed, the reactions responsible for product formation are confined within the individual micrometer-sized spherical droplets which act as individual chemical reactors. Particles are rough and polyhedral with irregular shapes and some degree of superficial porosity, especially when tungsten content is increased. These hollow particles probably originated from high internal stresses during particles formation and rapid evaporation of solvent from the surface, leading to the formation of twisted particles. Indeed, the faster evaporation rate as compared to solute diffusion results in a decreasing concentration gradient from the surface towards the center of the droplet, yielding precipitation at the surface rather than in the entire volume [23]. Surface precipitation is particularly significant for large droplet sizes, leading to the formation of a shell on the droplet surface, trapping a certain amount of solution inside the droplet eventually turning into void as the temperature increases which causes greater plastic deformation and shrinkage in the latter stages. No relation between average diameter size and tungsten content can be established since the differences observed for tungsten-doped samples are in the uncertainty range. Nevertheless, it can be seen that samples with higher tungsten content present a more homogeneous particle size distribution. The volumetric distribution of samples with low tungsten content is dominated by large spheres; for example, particles larger than  $1.5 \mu\text{m}$  represent more than 80 % of the whole volume for  $x=0$  and 89 % for  $x=0.5$ . This effect is decreased with further tungsten substitution, since particles larger than  $1.5 \mu\text{m}$  represent only 36 and 23 % of the whole

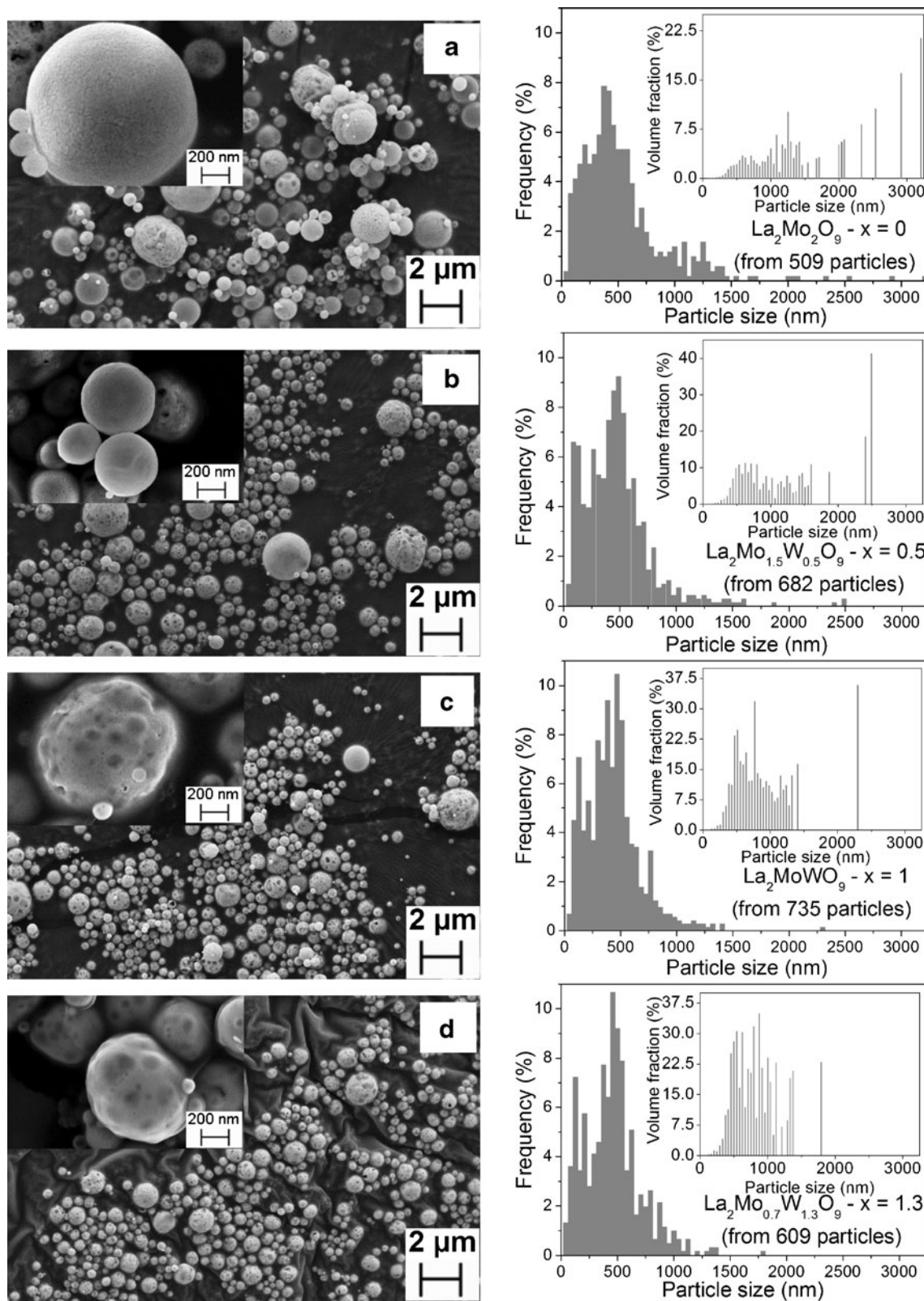


**Fig. 1** SEM images (*left*) and particle size and volumetric distribution (*right*) from  $\text{La}_2\text{Mo}_{2-x}\text{W}_x\text{O}_9$  powders with **a**  $x=0$ , **b**  $x=0.5$ , **c**  $x=1$ , and **d**  $x=1.3$

volume for  $x=1$  and 1.3, respectively. This tendency is in agreement with the more homogeneous particle size

distribution exhibited when tungsten content is increased.

**Table 1** Results from statistical analysis of  $\text{La}_2\text{Mo}_2 - x\text{W}_x\text{O}_9$  particles

$x$	Number of measured particles	Arithmetic average (nm)	Standard deviation (nm)	Mode (nm)
0	509	532	391	375
0.5	682	467	304	489
1	735	430	244	468
1.3	609	455	250	458

### Structural characterization of SP powders

Figure 2 displays the results obtained from  $\text{La}_2\text{Mo}_2 - x\text{W}_x\text{O}_9$  powder XRD data refinement. Experimental and calculated patterns, the difference between them, and the Bragg positions are shown in this figure. Table 2 summarizes the results obtained from the microstructural analysis. The cell parameters are in agreement with previous reports [4]. Pure  $\text{La}_2\text{Mo}_2\text{O}_9$  sample presents a mean crystallite size larger than those corresponding to tungsten-doped samples. Nevertheless, it is worth to note that at least part of this difference could be produced by substantial overlap and subsequent difficulty in deconvoluting properly individual reflections in the case of  $\text{La}_2\text{Mo}_2\text{O}_9$  phase. This phase crystallizes at room temperature as a monoclinic symmetry which represents a slight distortion from the cubic  $\text{La}_2\text{Mo}_2 - x\text{W}_x\text{O}_9$  phase with large  $2 \times 3 \times 4$  superstructure. For that reason, monoclinic  $\text{La}_2\text{Mo}_2\text{O}_9$  diffractogram presents reflection splitting as compared to cubic  $\text{La}_2\text{Mo}_2 - x\text{W}_x\text{O}_9$  diffractograms, with a lot of low-intensity additional peaks (not considered in the calculated profile). In addition, line profile broadening due to size effects causes a strong overlap between neighboring reflections in monoclinic  $\text{La}_2\text{Mo}_2\text{O}_9$ .

### Differential thermal and thermogravimetric analyses on SP powders

The thermal behavior of  $\text{La}_2\text{Mo}_2 - x\text{W}_x\text{O}_9$  samples under heating is displayed in DTA and TGA curves of Fig. 3. Mass losses between 0.8 and 1.8 % were observed in all cases. This behavior can be related to sample dehydration and to decomposition of organic precursors [24, 25] which were not decomposed during pyrolysis process. It is worth to note that these residual compounds could not be detected by XRD because of their small quantity and amorphous state. DTA curves show an endothermic peak at 564 °C for  $\text{La}_2\text{Mo}_2\text{O}_9$  and at a temperature between 540 and 545 °C for  $x=0.5, 1, \text{ and } 1.3$ . This peak can be associated to the  $\alpha/\beta$  transition [3] in the case of pure  $\text{La}_2\text{Mo}_2\text{O}_9$ . However, no  $\alpha/\beta$  transition is expected for  $\text{La}_2\text{Mo}_2 - x\text{W}_x\text{O}_9$  samples according to previous research works [3, 6]. Two consecutive heating and cooling cycles were recorded for an as-prepared  $\text{La}_2\text{Mo}_{1.5}\text{W}_{0.5}\text{O}_9$  sample (see Fig. 4) with the aim of determining if this peak is correlated to the decomposition of residual phases. TGA/DTA curves corresponding to

the first cycle are similar than those displayed in Fig. 3, although the mass loss is about one half, which is probably due to a different hydration degree. The TGA curve from the second cycle does not show any significant mass loss, indicating no presence of residual organic precursors after first heating cycle. Therefore, the endothermic peak observed at 557 °C in the second DTA curve (see Fig. 4(b)) should be related to some phase transition occurring in the  $\text{La}_2\text{Mo}_2 - x\text{W}_x\text{O}_9$  oxide. Similar endothermic peaks within the 450–700 °C temperature range were reported for  $\text{La}_2\text{Mo}_2\text{O}_9$ -based oxides doped with  $\text{Bi}^{3+}$ ,  $\text{Ca}^{2+}$ ,  $\text{Nd}^{3+}$ ,  $\text{Pr}^{3+}$  in the  $\text{La}^{3+}$  site, and  $\text{V}^{5+}$  in the  $\text{Mo}^{6+}$  site [26–31]. In some cases, these peaks were attributed to the transformation from a metastable  $\beta_{\text{ms}}$  phase to the high-temperature  $\beta$  phase involving a transition from static to dynamic oxygen disorder [26–28]. In other cases, these peaks were related to the coexistence of the  $\beta$  phase with small quantities of  $\alpha$  phase at room temperature and the system relaxation upon heating, leading to a topological metastability with successive  $\beta/\alpha/\beta$  transitions [29–31]. In addition, it was demonstrated that the  $\alpha/\beta$  equilibrium can be modified by the thermal history, the external stress, the internal strain, and the composition of the sample [26–31]. These phenomena could explain our results, although further investigations must be done in order to clarify this issue.

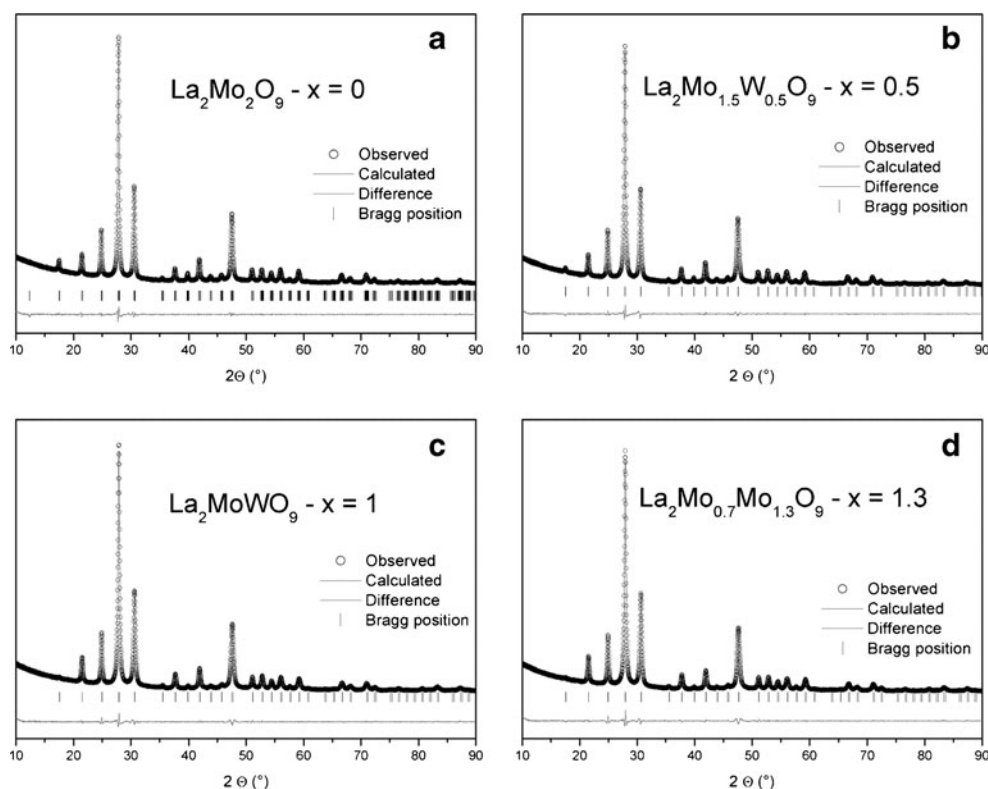
### Dilatometry

Figure 5 shows the shrinkage curves obtained from  $\text{La}_2\text{Mo}_2 - x\text{W}_x\text{O}_9$  green pellets in static air. The temperature at which shrinkage starts, maximum shrinkage rate is achieved, and shrinkage is completed depends on tungsten content, yielding higher temperatures for higher tungsten content. Shrinkage starts between ~615 °C (for  $x=0$ ) and ~810 °C (for  $x=1.3$ ), the maximum shrinkage rate is achieved between ~770 °C (for pure  $\text{La}_2\text{Mo}_2\text{O}_9$ ) and ~895 °C (for  $\text{La}_2\text{Mo}_{0.7}\text{W}_{1.3}\text{O}_9$ ), and shrinkage is completed between ~1,000 °C ( $x=0$ ) and ~1,130 °C ( $x=1.3$ ).

### Morphology of $\text{La}_2\text{Mo}_2 - x\text{W}_x\text{O}_9$ dense ceramics

SEM micrographs (left) and grain size and volumetric distributions (right) of polished and thermally etched ceramic surfaces are presented in Fig. 6. Figure 6a

**Fig. 2** Experimental and calculated patterns, the difference between them, and the Bragg positions from  $\text{La}_2\text{Mo}_{2-x}\text{W}_x\text{O}_9$  powder XRD data refinement for **a**  $x=0$ , **b**  $x=0.5$ , **c**  $x=1$ , and **d**  $x=1.3$



shows SSR00 pellet with average grain size of  $17\ \mu\text{m}$  with some visible pores. SP00 pellet (Fig. 6b) presents slightly smaller grains with an average value of  $8\ \mu\text{m}$  and lower porosity as compared to SSR00. In spite of the short sintering time (10 min), the SP00 grain growth is considerable, starting from SP powders with crystallite sizes in the 30–44 nm range. The SPS00 fractured cross-section, observed in Fig. 6c, shows a different microstructure than those of SSR00 and SP00. At the same magnification than the formers, smaller grains are visible as well as large rows of interconnected pores. The micrograph in the inset in Fig. 6c was taken with higher magnification, and the visible grains have an average size of  $\sim 250\ \text{nm}$ . This fine microstructure was achieved as a result of the applied spark plasma sintering in which the pellet reached a high temperature

for only some fractions of seconds. The measured relative density of this pellet was only 82 % (see Table 3). This agrees with the presence of close porosity in the bulk of the pellet which would affect the electrical values obtained for this ceramic as solid electrolyte.

Figure 6d, e shows the related SSR13 and SP13 micrographs, respectively. The SSR13 SEM image shows large grains ( $100\ \mu\text{m}$  in average) as a result of the high sintering temperature ( $1,300\ ^\circ\text{C}$ ) and relatively long sintering time (120 min). SP13 micrograph presents an average grain size of  $2.4\ \mu\text{m}$ . This value is considerably lower than that of SP00 pellet as a result of the even shorter sintering time (1 min). The relative density of SP13 pellet was 90 % (see Table 3). Statistic results of the measured grain sizes in SEM images are summarized in Table 3.

**Table 2** Results obtained from  $\text{La}_2\text{Mo}_{2-x}\text{W}_x\text{O}_9$  powder XRD data refinement

$x$	$d_{\text{mean}}$ (nm)	Anisotropy	Max. strain (%)	Anisotropy (%)	$a$ (Å)	$b$ (Å)	$c$ (Å)	$\beta$ (°)	$R_{\text{Bragg}}$	$R-F$
0	44	1.35	0.1665	0.0004	$7.1397 \pm 0.0003$	$7.1530 \pm 0.0001$	$7.1684 \pm 0.0003$	$89.705 \pm 0.003$	0.293	0.377
0.5	32.7	0.20	0.2297	0.0001	$7.15235 \pm 0.00009$	–	–	–	0.242	0.429
1	30.4	0.38	0.2521	0.0003	$7.14714 \pm 0.00009$	–	–	–	0.197	0.318
1.3	31.8	0.12	0.2637	0.0001	$7.13927 \pm 0.00009$	–	–	–	0.236	0.345

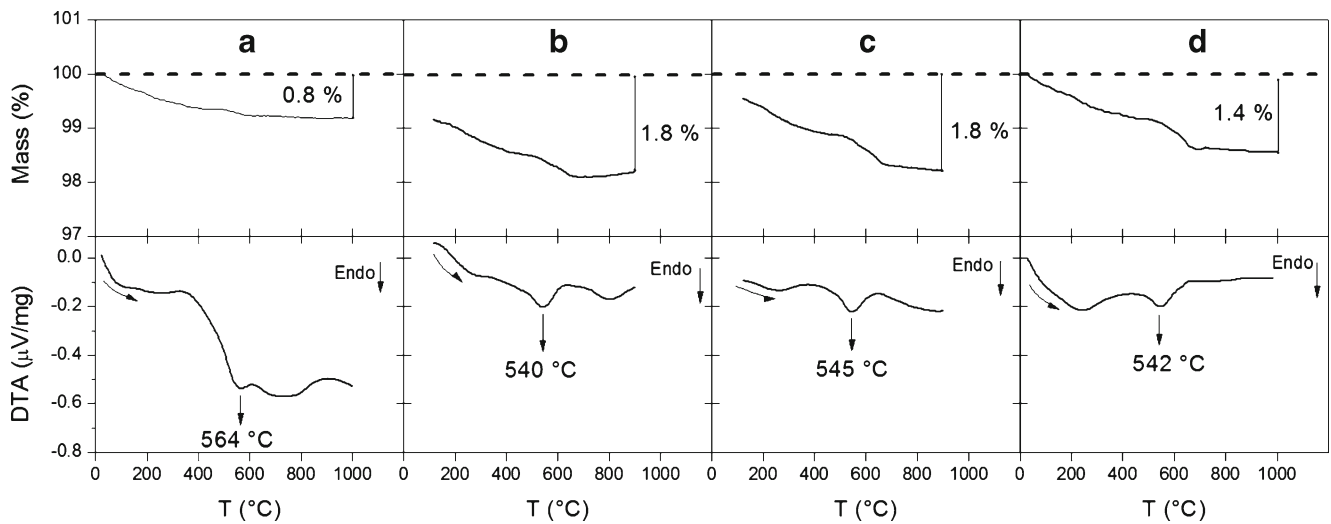


**Fig. 3** TGA (*top*) and DTA (*bottom*) data from  $\text{La}_2\text{Mo}_{2-x}\text{W}_x\text{O}_9$  with  $a\ x=0$ ,  $b\ x=0.5$ ,  $c\ x=1$ , and  $d\ x=1.3$  prepared by SP

Structural and microstructural characterization of dense pellets by XRD

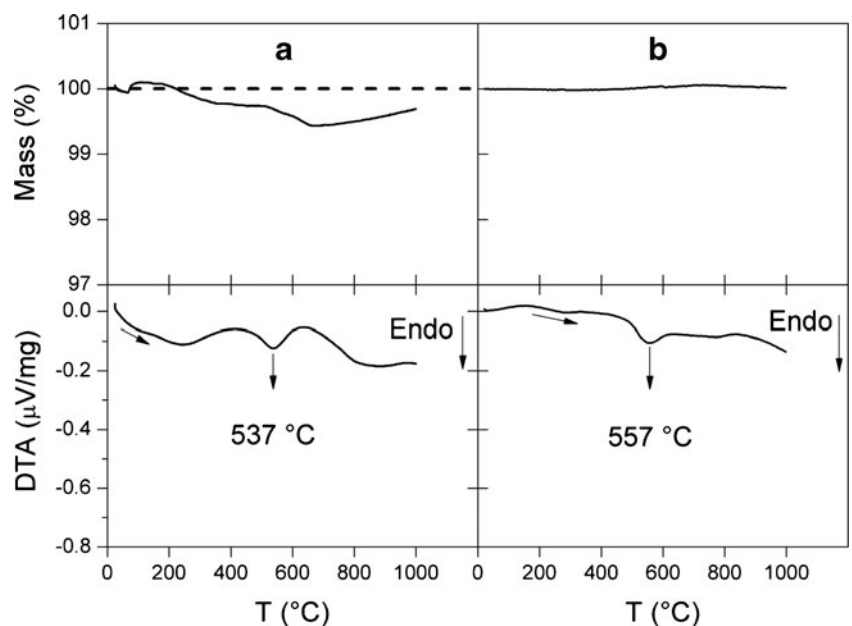
The XRD patterns obtained from SSR00, SP00, and SPS00 pellets are shown in Fig. 7a. The comparison between SSR00 and SP00 shows no significant difference or peak broadening, which is in good agreement with similar microstructure composed of micrometric grains found for both ceramics by SEM. On the other hand, SPS00 pattern exhibits a visible peak broadening as compared to SSR and SP00 (see inset in Fig. 7a) due to the fine microstructure as observed by SEM. Figure 7b shows the Rietveld refinement data for SPS00. An average grain size of 200 nm (with 0.11 % of maximum strain)

was determined from the microstructural analysis described elsewhere [14]. This average grain size is in good agreement with that observed by SEM (see Table 3). The estimation of both SSR00 and SP00 grain sizes was impossible due to the absence of peak broadening.

Electrical characterization

The normalized EIS spectra of SSR00, SP00, and SPS00 ceramics obtained after stabilization at  $\sim 362\text{ }^\circ\text{C}$  from 13 MHz to 5 Hz are shown in Fig. 8. The equivalent electrical models used to fit each spectrum are also shown. As usually observed for  $\text{La}_2\text{Mo}_2\text{O}_9$ -based ceramics, only

**Fig. 4** TGA (*top*) and DTA (*bottom*) data from  $\text{La}_2\text{Mo}_{1.5}\text{W}_{0.5}\text{O}_9$  powder for the *a* first and *b* second cycles



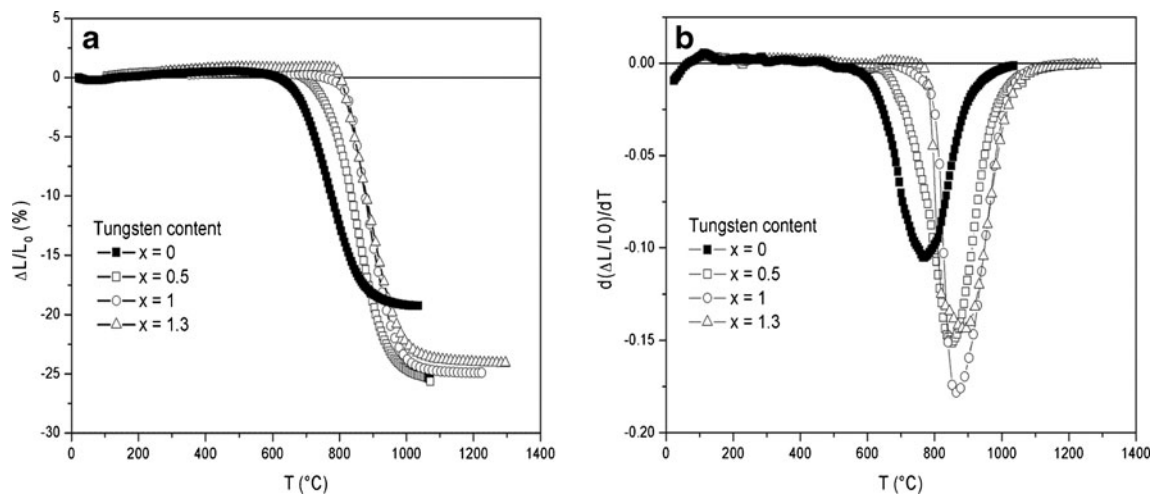


**Fig. 5** a Shrinkage and b shrinkage rate curves for  $\text{La}_2\text{Mo}_{2-x}\text{W}_x\text{O}_9$  ( $x=0, 0.5, 1$ , and  $1.3$ ) green pellets

one semicircle at high frequency is observed for both SSR00 and SP00 samples. Given the refined values of capacitances and relaxation frequencies, this high-frequency semicircle was attributed to the intragranular (bulk (B)) conduction process. As observed in Fig. 6 and mentioned in “Morphology of  $\text{La}_2\text{Mo}_{2-x}\text{W}_x\text{O}_9$  dense ceramics,” the microstructures of both SSR00 and SP00 pellets are quite similar. This is the reason why the EIS spectra are similar, and although the starting SP  $\text{La}_2\text{Mo}_2\text{O}_9$  powders was nanometric, the sintering process yielded micrometric grains for SP00 ceramic.

In the case of SPS00 pellet (Fig. 8, left down), a second semicircle appears in the Nyquist diagram at intermediate frequency. Two  $R||CPE$  were used to fit the EIS spectrum of SPS00 sample. The intermediate-frequency semicircle was assigned to an intergranular (grain boundary (GB)) conduction process. Given that the volume fraction of grain boundary is higher in SPS00 sample (with 250 nm average grain size) in comparison to SSR00 (with 17  $\mu\text{m}$  average grain size), the conduction path across the grain boundaries in SPS00 becomes comparable to that of the bulk. In other words, for microsized grains, the ceramics do not present any GB blocking effect (as usually observed for  $\text{La}_2\text{Mo}_2\text{O}_9$ -based ceramics).

For nanoscaled grains, the ceramics present a significant blocking effect observed at lower frequency related to high volumetric concentration of grain boundaries.

The comparison of the three normalized spectra of SSR00, SP00, and SPS00 at 362 °C is shown in Fig. 8, downright. The lowest resistivity value (distance between the origin and the intersection with real axis) is that of SSR00 sample. The values for both SP00 and SPS00 are equivalent and slightly higher than that of SSR00 sample because of the microstructure-related blocking effect.

Table 4 summarizes the electrical parameters such as resistivity  $\rho$ , capacity  $c$ , relaxation frequency  $\omega_0$ , and depression angles for both B and GB contributions for SPS00 at temperatures between 301 and 421 °C. These values were calculated from  $R$ , CPE, and  $p$  parameters obtained from the refinement of the theoretical models;  $k$  is the geometric factor (area/thickness) of each pellet.

$$C = \frac{(R \cdot \text{CPE})^{\frac{1}{p}}}{R}$$

$$c = \frac{C}{k}$$

$$\omega_0 = (RC)^{-1}$$

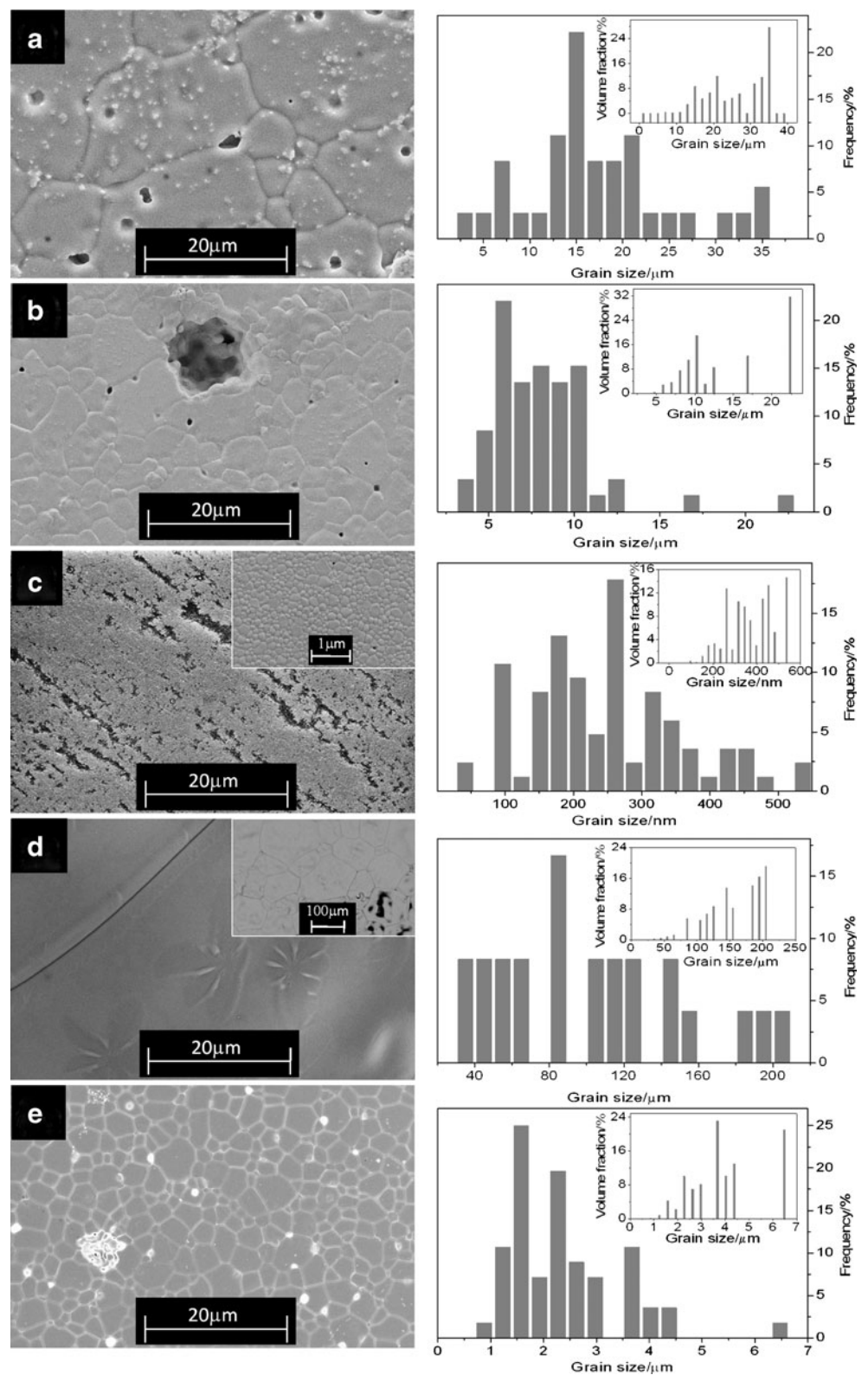
$$\frac{\pi}{2}(1-p)$$

The normalized spectra from SSR13 and SP13 samples with the relative density of the same order of magnitude (91–92 %) measured at 362 °C in air are shown in Fig. 9. Both spectra have similar shape with only one bulk semicircle. The difference between them is the diameter of the semicircle (therefore the resistivity values). When considering all the uncertainties (geometric factors, electrode areas, temperature during the electrical measurements...), the small difference between SSR13 and SP13 could not be considered as significant.

The electrical parameters for all the measured ceramics at ~362 °C in air are summarized in Table 5.

Arrhenius plots of conductivity obtained from EIS measurements for SSR00, SP00, SPS00, SSR13, and SP13 are

**Fig. 6** SEM images (*left*) and grain size and volumetric distribution (*right*) from  $\text{La}_2\text{Mo}_{2-x}\text{W}_x\text{O}_9$  ceramics: **a** SSR00, **b** SP00, **c** SPS00, **d** SSR13, and **e** SP13



presented in Fig. 10. For  $x=0$  samples (SSR00, SP00, and SPS00), the curves show the monoclinic( $\alpha$ ) $\leftrightarrow$ cubic( $\beta$ ) transition at  $\sim 580$  °C with the corresponding increase of conductivity values. Below the transition temperature, the

conductivity values are equivalent (see squares, circles, and triangles up). Above  $\sim 580$  °C, the three curves split slightly, SSR00 and SPS00 exhibiting the highest and the lowest values, respectively.

**Table 3** Geometric characteristics, sintering conditions, and average grain sizes determined by a statistical analysis from SEM observations of  $\text{La}_2\text{Mo}_2-x\text{W}_x\text{O}_9$  pellets

Pellet	W content $x$	Geometric factor $k = \frac{\text{Area}}{\text{Thickness}}$ (cm)	Sintering temperature (°C)	Sintering time (min)	Relative density (%)	Number of measured grains	Grain size arithmetic average ( $\mu\text{m}$ )	Grain size standard deviation ( $\mu\text{m}$ )
SSR00	0	4.92	1,070	120	91	36	17	8
SP00	0	3.10	970	10	92	59	8	3
SPS00	0	2.81 <sup>a</sup>	700	2	82	84	0.252	0.11
SSR13	1.3	4.21	1,300	120	90	24	101	50
SP13	1.3	3.12	1,090	1	90	56	2.4	1

<sup>a</sup> Due to the rough surface of the pellet obtained by SPS sintering, the thickness of the sample was probably slightly overestimated

The bulk (triangles left) and grain boundary (stars) contributions to the total ionic conductivity of SPS00 are also compared, in the 300 to 421 °C temperature range. It is worth to note that the GB conductivity values were obtained from arbitrarily normalizing the GB resistance values with the macroscopic geometric factor  $k$ . Arrhenius plots of relaxation frequencies of both the bulk  $\omega_0^{\text{B}}$  and the grain boundary  $\omega_0^{\text{GB}}$

contributions for SPS00 are shown in the inset of Fig. 10. The activation energies for each contribution are equivalent for both conductivity values and relaxation frequencies.

The curves corresponding to SSR13 and SP13 of close relative density (90, 92 %) are very similar. The activation energy in the whole temperature range is the same for both (1.43 eV). This fact confirms the intrinsic character of the bulk conductivity in these compounds, which does not vary despite the big differences in average grain sizes (see Fig. 6e, f and Table 3).

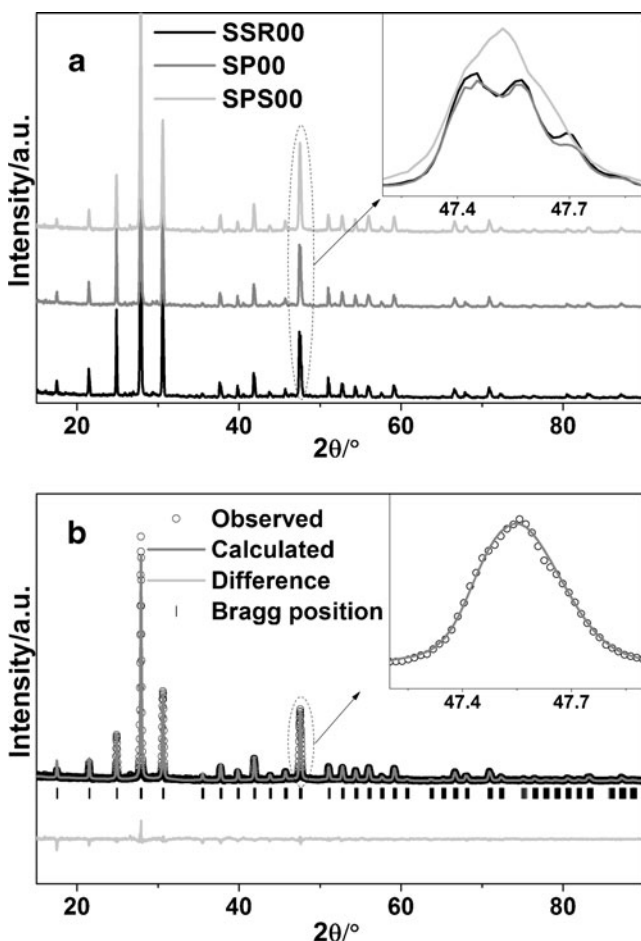


**Fig. 7** a XRD patterns of SSR00, SP00, and SPS00 pellets. b Rietveld refinement for SPS00 diffractogram. The peak at about  $2\theta=47.55^\circ$  is zoomed in the inset

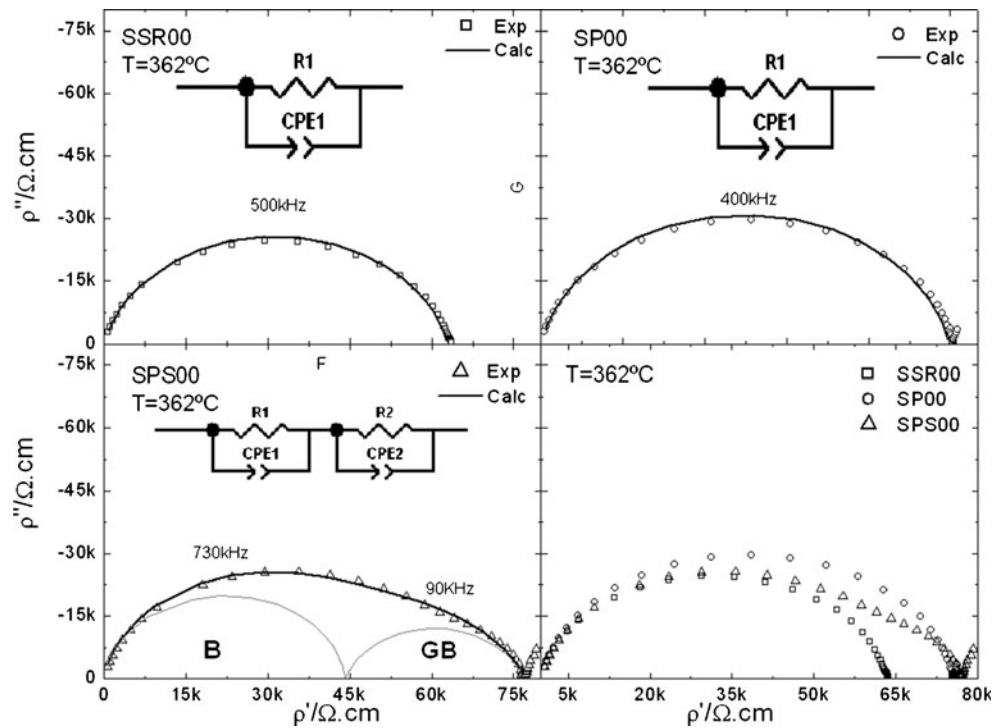
## Discussion

SP  $\text{La}_2\text{Mo}_2-x\text{W}_x\text{O}_9$  powders analyzed in this work present crystallite sizes of 30–33 nm for  $x=0.5, 1.0,$  and  $1.3$  and of  $\sim 44$  nm for  $x=0$  and particle sizes of 430–530 nm. Crystallite size of pure  $\text{La}_2\text{Mo}_2\text{O}_9$  powders is somewhat larger than those previously reported (i.e.,  $\sim 27$  nm) for  $\text{La}_2\text{Mo}_2\text{O}_9$  powders obtained by spray pyrolysis in the same conditions (i.e., solution concentration, 0.025 M; ultrasonic frequency, 1.7 MHz; flow rate,  $6 \text{ L min}^{-1}$ ; temperature, 600 °C) but starting from  $\text{La}_2\text{O}_3$  and  $\text{MoO}_3$  precursors [14]. This would indicate that solution precursors have some influence on crystallite size. Indeed, powder morphology varies with respect to the precursor solubility. In addition,  $\alpha/\beta$  transition temperature in the pure  $\text{La}_2\text{Mo}_2\text{O}_9$  samples (i.e., 564 °C) is higher than that reported in Georges et al. [14] (i.e., 545 °C) due to the smaller crystallite size of the latter one. Nevertheless,  $\alpha/\beta$  transition temperature reported here is still lower than the one corresponding to  $\text{La}_2\text{Mo}_2\text{O}_9$  prepared by a solid-state reaction (i.e., 580 °C) [3].

DTA curves for W-doped samples present an unidentified peak in the 540–545 °C range. Since it is not expected that this peak relates to  $\alpha/\beta$  transition for  $\text{La}_2\text{Mo}_2-x\text{W}_x\text{O}_9$  [3, 6], further investigation must be done in order to explain this observation.

On the other hand, particle sizes of pure  $\text{La}_2\text{Mo}_2\text{O}_9$  powders are in a similar range than those observed for analogous powders in Georges et al. [14]. Shrinkage starts

**Fig. 8** Nyquist plots of EIS spectra from SSR00, SP00, and SPS00 ceramics at 362 °C in air from 13 MHz to 5 Hz



at similar temperature (i.e., ~600 °C) for both samples as expected, since they have identical composition and similar particle sizes [32]. Shrinkage is completed at a temperature of ~100 °C lower for powders prepared from oxide precursors [14], indicating that their particle size distribution would allow a dense packaging of spheres in green pellets and would facilitate sintering process [32].

W-rich solutions would have some tendency to form smaller particles when they are atomized, leading to narrower particle size distribution of  $\text{La}_2\text{Mo}_{2-x}\text{W}_x\text{O}_9$  powders. This can be explained by the density increase with tungsten content, since aerosol droplet size is inversely proportional to the density of the solution [33]. According to Lang's equation, the mean diameter of the aerosol droplets ( $D$  in micrometer) is link to the surface tension of the atomized solution ( $\sigma$  in gram per cubic centimeter), the density of the solution ( $\delta$  in gram per cubic centimeter),

and the ultrasonic frequency of the piezoelectric ceramic transducers ( $f$  in hertz) [33]:

$$D = 0.34 \times 10^6 \left( \frac{8\pi\sigma}{\delta f^2} \right)^{\frac{1}{3}}$$

Temperatures at which shrinkage begins, maximum shrinkage rate is achieved, and shrinkage is completed increase with tungsten content as it was also observed by other authors [5]. This behavior can be attributed to the higher temperatures needed for diffusion of heavier tungsten atoms. Additionally, the finest microstructure achieved using a spray pyrolysis technique has allowed reducing the sintering temperature with respect to those usually reported for a solid-state reaction method [12, 13]. The shrinkage behavior of  $\text{La}_2\text{Mo}_{2-x}\text{W}_x\text{O}_9$  powders observed in this work is similar to that reported for W-doped LAMOX powders

**Table 4** Resistivity, capacity, relaxation frequency, and depletion angle for both bulk (B) and grain boundary (GB) contribution for SPS00 at temperatures between 301 and 421 °C

T (°C)	$\rho^B$ (Ω cm)	$c^B$ ( $10^{-12}$ F $\text{cm}^{-1}$ )	$\omega_0^B$ ( $10^6$ rad $\text{s}^{-1}$ )	$\beta^B$ (°)	$\rho^{GB}$ (Ω cm)	$c^{GB}$ ( $10^{-11}$ F $\text{cm}^{-1}$ )	$\omega_0^{GB}$ ( $10^5$ rad $\text{s}^{-1}$ )	$\beta^{GB}$ (°)
301	263,737	4.88	0.78	7.29	197,389	8.15	0.62	15.07
330	112,284	4.99	1.79	7.12	80,659	6.91	1.79	15.86
357	52,548	5.18	3.67	6.43	39,032	5.20	4.92	16.26
364	43,927	5.20	4.37	5.61	32,524	5.47	5.62	16.87
391	19,925	5.67	8.85	2.29	18,627	3.69	14.5	16.80
421	11,076	5.92	15.2	1.95	7,300	5.44	25.2	15.30

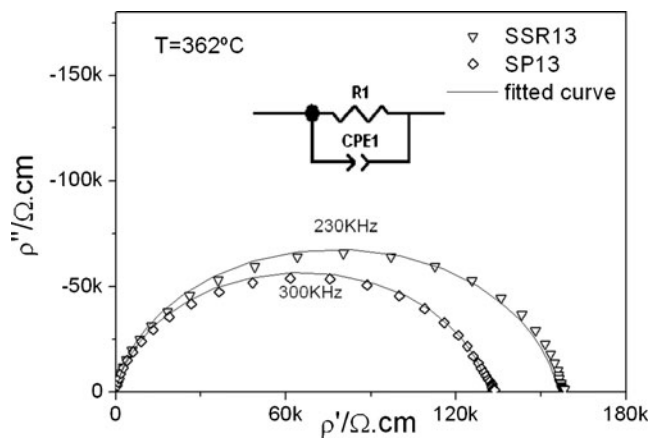


**Fig. 9** Nyquist plots of EIS spectra from SSR13 and SP13 ceramics at 362 °C in air

prepared using a freeze-drying method [5], but with the advantage of using a low-cost, simpler, and faster synthesis method consisting in a one-step process.

Marrero-Lopéz et al. have observed that  $\text{La}_2\text{Mo}_2\text{O}_9$  obtained using a freeze-dried precursor method and sintered below 925 °C presented poor ionic conductivity values in spite of having relative densities above 92 % [16]. They claim that this behavior may be due to a poor connectivity between grains in these ceramics. In our case, the grains are well connected as shown in the inset of Fig. 6c, but a large zone of porosity was found yielding a density of only 82 %. Yang et al. who have sintered  $\text{La}_2\text{Mo}_2\text{O}_9$  ceramics by SPS with good homogeneity have found better conductivity values for SPS pellets as compared to those of conventionally sintered ones [34]. Nevertheless, in the cited work, the relative densities obtained for SPS samples are at least 90 % (and rather higher), whereas for conventionally sintered ones, only 78 %.

The lower polarization resistances measured in this work for SP13 as compared to SSR13 (see Fig. 9) might be related to the smaller average grain size of 2.4  $\mu\text{m}$ , as compared to that of SSR13 of 101  $\mu\text{m}$ . This observation is consistent with some results reported by Wang et al. for  $\text{La}_2\text{Mo}_2\text{O}_9$  samples prepared using the

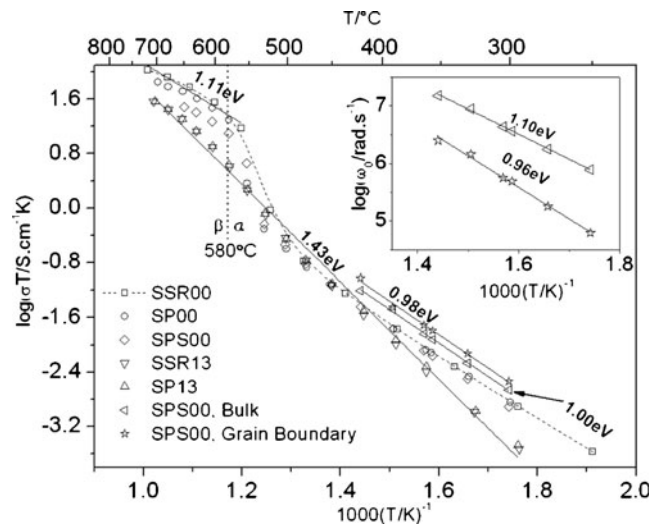


**Fig. 10** Arrhenius plots of measured ionic conductivities for SSR00, SP00, SPS00, SSR13, and SP13. The relaxation frequencies for bulk (HF) and grain boundary (MF) for SPS00 pellet are shown in the inset

Pechini method [8]. They found that samples with grain sizes within 0.8–5  $\mu\text{m}$  range exhibit ionic conductivity values two to five times higher than those corresponding to macrocrystalline samples.

Georges et al. compared the electrical features of  $\text{La}_2\text{Mo}_2\text{O}_9$  ceramics with different microstructures [14]. They found that  $c$  and  $\omega$  had similar values for the high frequency semicircles (bulk contribution) regardless of the grain size or the presence or absence of an intermediate-frequency semicircle, at a given temperature. In the present work, this behavior is also observed for the three  $x=0$  and the two  $x=1.3$  pellets. This agreement confirms that the diminution of grain size, at least up to the values obtained in this work for  $\text{La}_2\text{Mo}_2-x\text{W}_x\text{O}_9$  ceramics, does not affect the intrinsic bulk behavior of these materials, but it only increases the contribution of the grain boundary blocking effect. Although the total resistivity values for pellets with the same composition are in the same magnitude order, slight differences are observed (see Figs. 8 and 9). The influence of the grain size in these resistivity values is strongly dependent on the relative density of the pellets with same composition and grain size (see Table 3).

**Table 5** Electrical parameters obtained from EIS spectra for ceramic samples at  $\sim 362$  °C in air

Pellet	$\rho^B$ ( $\Omega$ cm)	$c^B$ ( $10^{12}$ F $\text{cm}^{-1}$ )	$\omega_0^B$ ( $10^6$ rad $\text{s}^{-1}$ )	$\beta^B$ ( $^\circ$ )	$\rho^{GB}$ ( $\Omega$ cm)	$c^{GB}$ ( $10^{-11}$ F $\text{cm}^{-1}$ )	$\omega_0^{GB}$ ( $10^5$ rad $\text{s}^{-1}$ )	$\beta^{GB}$ ( $^\circ$ )
SSR00	64,134	5.02	3.11	13.98				
SP00	76,397	4.86	2.69	13.63				
SPS00	43,927	5.20	4.37	5.61	32,524	5.47	5.62	16.87
SSR13	158,661	4.14	1.52	10.06				
SP13	132,715	4.2	1.79	10.58				

## Conclusions

$\text{La}_2\text{Mo}_2 - x\text{W}_x\text{O}_9$  ( $x=0, 0.5, 1.0,$  and  $1.3$ ) nanocrystalline powders were prepared using a spray pyrolysis technique, with  $\text{La}(\text{NO}_3)_3 \cdot 6 \text{H}_2\text{O}$ ,  $(\text{NH}_4)_6\text{Mo}_7\text{O}_{24} \cdot 4 \text{H}_2\text{O}$ , and  $(\text{NH}_4)_6\text{W}_{12}\text{O}_{39} \cdot \gamma \text{H}_2\text{O}$  as precursors. The obtained powders present spherical morphology with particles sizes from 430 to 530 nm and crystallite sizes in the 30–44 nm range. Particle size distribution becomes more homogeneous with higher tungsten content. In addition, shrinkage behavior of  $\text{La}_2\text{Mo}_2 - x\text{W}_x\text{O}_9$  powders depends on tungsten content, yielding to higher temperatures for W-richer samples. Sintering temperatures obtained using a spray pyrolysis technique are lower than those reported for a solid-state reaction [12, 13].

$\text{La}_2\text{Mo}_2 - x\text{W}_x\text{O}_9$  with  $x=0$  and 1.3 ceramics, obtained from powders prepared by SSR and SP, were sintered by conventional and SPS sintering and characterized by SEM, XRD, and EIS. Different sintering methods lead to pellets with average grain sizes ranging from 250 nm to 101  $\mu\text{m}$  and densities higher than 90 % of  $d_{\text{th}}$ . The smallest average grain size value of 252 nm was obtained by SPS. The notorious differences in morphology did not yield important variations of the electrical properties among samples of the same composition. A slight decrease of the conductivity was found for the sample obtained by SPS, related to a blocking effect due to high volumetric concentration of grain boundaries.

**Acknowledgments** The authors are grateful to acknowledge the A07E03 Cooperation Program ECOS-SUD. L. B. thanks Cécile Rossignol from the LEPMI for her assistance on spray pyrolysis synthesis.

## References

- EG&G Technical Services, Inc (2004) Fuel cell handbook, 7th edn. National Energy Technology Lab. US Department of Energy, Morgantown
- Skinner SJ, Kilner JA (2003) Ion conductors. *Materials Today* 6:30–37
- Lacorre P, Goutenoire F, Bohnke O, Retoux R, Laligant Y (2000) Designing fast oxide-ion conductors based on  $\text{La}_2\text{Mo}_2\text{O}_9$ . *Nature* 404:856–8
- Georges S, Goutenoire F, Laligant Y, Lacorre P (2003) Reducibility of fast oxide-ion conductors  $\text{La}_2 - x\text{R}_x\text{Mo}_2 - y\text{W}_y\text{O}_9$  ( $\text{R}=\text{Nd}, \text{Gd}$ ). *J Mater Chem* 13:2317
- Marrero-López D, Canales-Vázquez J, Ruiz-Morales J, Irvine J, Núñez P (2005) Electrical conductivity and redox stability of  $\text{La}_2\text{Mo}_2 - x\text{W}_x\text{O}_9$  materials. *Electrochim Acta* 50:4385–4395
- Goutenoire F, Isnard O, Suard E, Bohnke O, Laligant Y, Retoux R et al (2001) Structural and transport characteristics of the LAMOX family of fast oxide-ion conductors, based on lanthanum molybdenum oxide  $\text{La}_2\text{Mo}_2\text{O}_9$ . *J Mater Chem* 11:119–124
- Zhuang Z, Wang XP, Li D, Zhang T, Fang QF (2009) Ionic conductivity enhancement of  $\text{La}_2\text{Mo}_2 - x\text{W}_x\text{O}_9$  nanocrystalline films deposited on alumina substrates by the sol–gel method. *J Am Ceram Soc* 92:839–844
- Wang J, Wang Q, Wang X, Li C, Fang Q (2008) Synthesis and characterization of fine grained high density  $\text{La}_2\text{Mo}_2\text{O}_9$ -based oxide-ion conductors. *J Mater Sci Technol* 24:761–765
- Abdala PM, Custo GS, Lamas DG (2010) Enhanced ionic transport in fine-grained scandia-stabilized zirconia ceramics. *Journal of Power Sources* 195:3402–3406
- Bellino MG, Lamas DG, Walsøe de Reça NE (2006) Enhanced ionic conductivity in nanostructured, heavily doped ceria ceramics. *Adv Funct Mater* 16:107–113
- Corbel G, Laligant Y, Goutenoire F, Suard E, Lacorre P (2005) Effects of partial substitution of  $\text{Mo}^{6+}$  by  $\text{Cr}^{6+}$  and  $\text{W}^{6+}$  on the crystal structure of the fast oxide-ion conductor structural effects of  $\text{W}^{6+}$ . *Chem Mater* 17:4678–4684
- Georges S, Bohnke O, Goutenoire F, Laligant Y, Fouletier J, Lacorre P (2006) Effects of tungsten substitution on the transport properties and mechanism of fast oxide-ion conduction in  $\text{La}_2\text{Mo}_2\text{O}_9$ . *Solid State Ionics* 177:1715–1720
- Wang XP, Li D, Fang QF, Cheng ZJ, Corbel G, Lacorre P (2006) Phase transition process in oxide-ion conductor  $\beta\text{-La}_2\text{Mo}_2 - x\text{W}_x\text{O}_9$  assessed by internal friction method. *Appl Phys Lett* 89:021904
- Georges S, Rocha RA, Djurado E (2008) Microstructure related conductivity in  $\text{La}_2\text{Mo}_2\text{O}_9$  ceramics. *J Phys Chem C* 112:3194–3202
- Yang J, Wen Z, Gu Z, Yan D (2005) Ionic conductivity and microstructure of solid electrolyte  $\text{La}_2\text{Mo}_2\text{O}_9$  prepared by spark-plasma sintering. *J Eur Ceram Soc* 25:3315–3321
- Marrero-López D, Canales-Vázquez J, Ruiz-Morales J, Rodríguez A, Irvine J, Núñez P (2005) Synthesis, sinterability and ionic conductivity of nanocrystalline  $\text{La}_2\text{Mo}_2\text{O}_9$  powders. *Solid State Ionics* 176:1807–1816
- Rocha RA, Muccillo ENS (2003) Synthesis and thermal decomposition of a polymeric precursor of the  $\text{La}_2\text{Mo}_2\text{O}_9$  compound. *Chem Mater* 15:4268–4272
- Le Bail A, Duroy H, Fourquet JL (1988) Ab-initio structure determination of  $\text{LiSbWO}_6$  by X-ray powder diffraction. *Mater Res Bull* 23:447–452
- Rodríguez-Carvajal J (1993) Recent advances in magnetic structure determination by neutron powder diffraction. *Physica B* 192:55–69
- Rodríguez-Carvajal J (2001) An introduction to the program Fullprof 2000. Laboratoire Leon Brillouin, France
- Goutenoire F, Isnard O, Retoux R (2000) Crystal structure of  $\text{La}_2\text{Mo}_2\text{O}_9$ , a new fast oxide-ion conductor. *Chem Mater* 12:2575–2580
- Djurado E, Meunier E (1998) Synthesis of doped and undoped nanopowders of tetragonal polycrystalline zirconia (TPZ) by spray-pyrolysis. *Journal of Solid State Chemistry* 141:191–198
- Messing GL, Zhang S-C, Jayanthi GV (1993) Ceramic powder synthesis by spray pyrolysis. *J Am Ceram Soc* 76:2707–2726
- Princivalle A, Perednis D, Neagu R, Djurado E (2004) Microstructural investigations of nanostructured  $\text{La}(\text{Sr})\text{MnO}_3 - \delta$  films deposited by electrostatic spray deposition. *Chem Mater* 16:3733–3739
- Shaheen WM, Selim MM (2000) Thermal decompositions of pure and mixed manganese carbonate and ammonium molybdate tetrahydrate. *J Therm Anal Calorim* 59:961–970
- Voronkova V, Kharitonova E, Krasilnikova A (2009) Phase transitions and electrical conductivity of Bi-doped  $\text{La}_2\text{Mo}_2\text{O}_9$  oxide ion conductors. *Phys Status Solidi A* 206:2564–2568
- Voronkova VI, Kharitonova EP, Orlova EI, Belov DA (2012) Extending the family of oxygen ion conductors isostructural with  $\text{La}_2\text{Mo}_2\text{O}_9$ . *J Solid State Chemistry* 196:45–51
- Voronkova VI, Kharitonova EP, Krasilnikova AE (2010) Specific features of phase transitions and the conduction of  $\text{La}_2\text{Mo}_2\text{O}_9$

- oxide-ion conducting compound doped with vanadium. *Crystallography Reports* 55:276–282
29. Selmi A, Corbel G, Kojikian S, Voronkova V, Kharitonova E, Lacorre P (2008) Complex effect of partial substitution of  $\text{La}^{3+}$  by  $\text{Ca}^{2+}$  on the stability of fast oxide-ion conductor  $\text{La}_2\text{Mo}_2\text{O}_9$ . *Eur J Inorg Chem* 11:1813–1821
  30. Corbel G, Durand P, Lacorre P (2009) Comprehensive survey of  $\text{Nd}^{3+}$  substitution in  $\text{La}_2\text{Mo}_2\text{O}_9$  oxide-ion conductor. *J Solid State Chemistry* 182:1009–1016
  31. Corbel G, Chevereau E, Kodjikian S, Lacorre P (2007) Topological metastability and oxide ionic conduction in  $\text{La}_{2-x}\text{Eu}_x\text{Mo}_2\text{O}_9$ . *Inorg Chem* 46:6395–6404
  32. Chiang Y-M, Birnie DP, Kingery WD (1997) *Physical ceramics: principles for ceramic science and engineering*. Wiley, Chichester
  33. Lang RJ (1962) Ultrasonic atomization of liquids. *J Acoust Soc Am* 34:6
  34. Yang J, Gu Z, Wen Z, Yan D (2005) Preparation and characterization of solid electrolytes  $\text{La}_{2-x}\text{A}_x\text{Mo}_{2-y}\text{W}_y\text{O}_9$  (A=Sm, Bi). *Solid State Ionics* 176:523–530